

# 3D Reconstruction of Highly Fragmented Bone Fractures

Andrew Willis<sup>†</sup>, Donald Anderson<sup>‡</sup>, Thad Thomas<sup>‡</sup>, Thomas Brown<sup>‡</sup>, J. Lawrence Marsh<sup>‡</sup>

<sup>†</sup>UNC - Charlotte, 9201 University City Blvd., Charlotte, NC 28223

<sup>‡</sup>The University of Iowa, 2181 Westlawn Building, Iowa City, IA 52242

## ABSTRACT

A system for the semi-automatic reconstruction of highly fragmented bone fractures, developed to aid in treatment planning, is presented. The system aligns bone fragment surfaces derived from segmentation of volumetric CT scan data. Each fragment surface is partitioned into intact- and fracture-surfaces, corresponding more or less to cortical and cancellous bone, respectively. A user then interactively selects fracture-surface patches in pairs that coarsely correspond. A final optimization step is performed automatically to solve the N-body rigid alignment problem. The work represents the first example of a 3D bone fracture reconstruction system and addresses two new problems unique to the reconstruction of fractured bones : (1) non-stationary noise inherent in surfaces generated from a difficult segmentation problem and (2) the possibility that a single fracture surface on a fragment may correspond to many other fragments.

**Keywords:** 3D reconstruction, bone segmentation, surface registration, CT



**Figure 1.** Radiographs of a range of comminuted tibial pilon fractures, varying in the number of bone fragments, the amount of fragment dispersal and the degree of intra-articular extension into the ankle.

## 1. PURPOSE

Severe limb trauma often leaves patients with highly fragmented bones, requiring surgical reconstruction. Obtaining an accurate restoration of the original unbroken bone from its fragments is a critical factor in determining the clinical prognosis, particularly in those cases where the fracture extends into an articular joint such as the knee or ankle. This paper presents a system for semi-automatic virtual reconstruction of bone fractures from volumetric CT data.

Extremity injuries that involve comminuted bone fractures almost always occur as a result of high-energy trauma such as from vehicular accidents or falls from a height. Beyond stabilization, treatment goals include achieving expeditious bony union in a position of acceptable limb alignment, and avoiding **Post-Traumatic**

---

Further author information: (Send correspondence to A. Willis)

A. Willis: E-mail: arwillis@uncc.edu, Telephone: 1 704 687 8420

D. Anderson: E-mail: don-anderson@uiowa.edu, Telephone: 1 319 335 8135

**OsteoArthritis (PTOA)** when there is extension into an articular joint. As a point of reference, for axial “pilon” fractures of the distal tibial articular surface (Figure 1), the incidence of PTOA of the ankle is in the range of 60% to 80%.<sup>1,2</sup>

Post-traumatic OA is a serious health condition that often leads to substantial pain, disability, loss of work, and decreased general health status. Its overall adverse impact on an individual’s physical and psychological well-being is comparable to that of other major disorders such as stroke, heart disease, or diabetes.<sup>3</sup> The societal cost of PTOA is high (estimated at \$12 billion/year in the U.S.),<sup>4</sup> since pain and loss of function frequently leads to loss of work capacity. Severe articular fractures most commonly occur in young adult patients. If PTOA develops, patients may require reconstructive surgery, including major procedures such as joint fusion or joint replacement. When these procedures are performed in a young patient, repeat surgeries throughout their lifetime may be necessary to maintain function, further raising the cost, and in some cases resulting in long term disability and unemployment.

Literature regarding semi-automatic or completely automatic reconstruction of bone fragments is surprisingly sparse given the very large body of research on the topic of bone segmentation, medical image registration,<sup>5,6</sup> and surface registration.<sup>7-10</sup> Ron *et al.* reported a computerized bone reconstruction system, but it was restricted to simple two-fragment fractures.<sup>11</sup> This paper extends recently developed techniques from the computer vision and computer graphics community for reconstructing broken archaeological artifacts<sup>12-14</sup> for application to reconstructing highly fragmented bone fractures. While some of these techniques are directly applicable to bone reconstruction, there are many new challenges. We address the following two significant challenges in this paper:

**Noise**— (CT data are less accurate than laser scan data and segmentation of the CT data amplifies noise in an unpredictable manner)

Archaeological fragment reconstruction algorithms typically use laser scan data which provide surface measurements with errors  $\leq 0.22mm$  in any direction<sup>15</sup> or significantly better, e.g.,  $\leq 0.04mm$  for the ShapeGrabber scanner.<sup>16</sup> The noise for these measurements is typically the same in any single direction, which makes them well suited for algorithms that are optimal for spherically symmetric (isotropic) noise conditions.

Volumetric CT data from clinical applications typically have a resolutions of approximately  $0.2 - 0.5mm$  in the plane of acquisition, and slightly larger ( $0.3 - 0.5mm$ ) in the direction along which images are acquired.<sup>17</sup> In addition, CT scan data reflect an averaging of tissue density over a finite slice volume/thickness, with associated partial volume artifacts. Extracting surfaces from volumetric CT data involves solving a difficult segmentation problem. As a result, surfaces segmented from CT data exhibit significantly more variability than is present in laser scan data. Additionally, this noise is non-stationary, i.e., it may be substantially more pronounced in difficult segmentation regions; further, the structure of this noise is dependent on biases present in the underlying surface-extraction segmentation algorithm.

**Fracture Generation Process** — (Bones break differently than archaeological artifacts)

Since archaeological artifacts are typically not constructed of bone, and certainly not living bone tissue, the generative fracture processes for ancient artifacts and bone tissue are somewhat different. Archaeological fragments typically consist of a hard brittle material such as stone, ceramic, or glass. In these cases fracture-surfaces may often, but not always, be extracted by locating ridges and discontinuities on the fragment surface. *The extracted fracture surfaces are then assumed to correspond to a single fracture surface from another fragment..* Note that this assumes that segmented fracture surfaces have a 1-to-1 correspondence, i.e., *a fracture surface extracted from a given fragment is assumed to match with one and only one other fracture surface from some other fragment.*

In contrast, living bone tends to splinter when subjected to high-energy trauma, generating pieces that not uncommonly have a single, smoothly varying fracture surface that may correspond to one, two or more fragments. For the studied tibial pilon fractures, we found that the proximal end of the remaining intact portion of the tibia (our *base fragment*) typically presented the largest fracture surface. Many other fragments share smooth surface regions that, when reconstructed, match with both the large tibial base fragment and with other smaller fragments (see Figure 1).

As a direct consequence of these differences in fracture behavior, the fracture surface correspondence assumptions for archaeological artifacts can be *much* more restrictive than those for bone reconstruction. Specifically, the bone reconstruction algorithm must allow for fracture-surfaces that are not 1-to-1, i.e., typical bone fragments may have multiple fracture-surfaces, and each fracture-surface may *partially match* with some other *partial* fracture-surface from another bone fragment. In some cases, there are fracture-surface regions that do not strictly have a compatible match. This may occur when segmentation variability leads to open gaps or interpenetrating surfaces when the fragment surfaces are properly aligned elsewhere. This makes the surface matching stage for bone reconstruction much more difficult than reconstruction of archaeological objects and precludes application of 1-to-1 surface matching techniques such as those proposed by Huang *et al.*<sup>14</sup>

## 2. METHODS

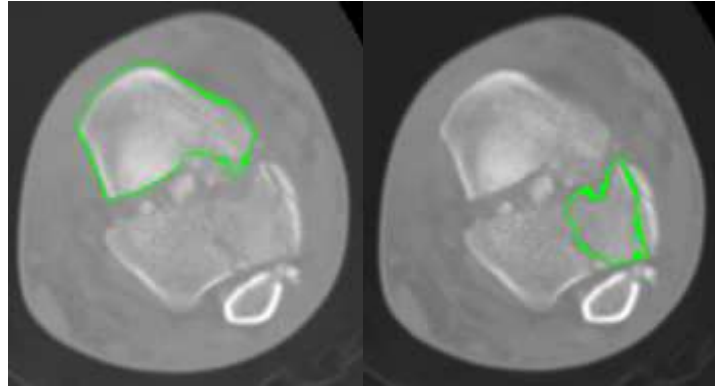
The system is divided into four parts:

1. Segment the volumetric CT data,<sup>17</sup> with an emphasis on generating discrete closed surfaces, i.e., fragment surfaces that may later be aligned (see §2.1).
2. Generate a surface mesh for each segmented bone fragment, and map each point on the surface mesh to a Hounsfield intensity (for the 3D surface point  $\mathbf{x}_i$  this map is referred to as  $f(\mathbf{x}_i)$ ) from the 3D CT scan volume  $\mathbf{I}(x, y, z)$  using a 3D *max()* filter centered about the voxel containing back-projection of each 3D fragment surface point into the CT scan volume (see §2.2).
3. Segment fragment surfaces into intact- and fracture-surfaces using intensities from step 2 (see §2.3).
4. Coarsely identify matching patches over contiguous fracture-surface regions, utilizing an interactive user interface. Optimize the specified fragment alignments to reconstruct the original bone from the bone fragments, using the interactively specified regions (see §2.4).

### 2.1. CT Data Segmentation

CT studies were obtained from twenty-two tibial pilon fracture cases, with axial in-plane resolutions ranging from 0.2 to 0.5 mm and slice spacing of 0.3 or 0.5 mm. This research was carried out with Institutional Review Board approval, and informed consent was obtained from all subjects. Fracture fragment boundaries were identified slice-by-slice from CT datasets using validated digital image analyses.<sup>17, 18</sup> A full 3D segmentation was completed in five of the cases using purpose-written code in MATLAB (The MathWorks, Inc., Natick, MA).

Bone surface segmentations within each slice provide noisy estimates of true surface geometries. The segmentation algorithm applied is not linear, which complicates the relation between the known (or possibly estimated) noise distributions present in the measured CT (Hounsfield) intensities and the noise present in the spatial positions of the segmented surface locations. Hence,  $(x, y)$  positions from the segmented CT slices are seen as noisy estimates of the true surface geometry, where each point has a unique unknown noise distribution.



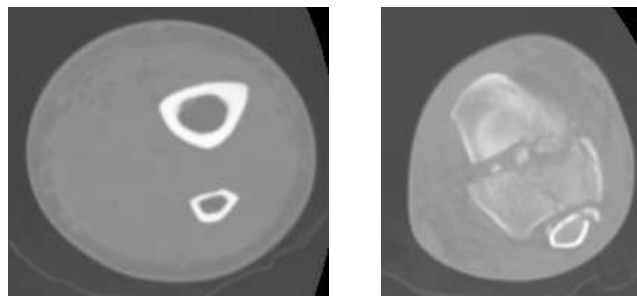
(a)

(b)

**Figure 2.** These two CT slices from a comminuted fracture of the distal tibia typify the challenges in estimating the location of bone fragment fracture-surfaces. The intersection of a segmented bone surface with the image slice is depicted in green for each image. Figure (a) depicts a situation where the apparent bone interior has higher intensity than that of the cortex, owing to the proximity to the subchondral bone underlying the ankle articular surface. Figure (b) depicts a situation where the estimated surface segmentation lies away from the true location of the cortical surface.

## 2.2. Using CT Intensities to Detect Fracture Surfaces

In this section, we present our techniques for identifying the subset of segmented surface points that correspond to fracture surfaces, i.e., surface regions generated when bone fragments have broken apart. To do so, for each 3D surface point  $\mathbf{x}_i = (x, y, z)^t$  we estimate a Hounsfield intensity denoted  $f(\mathbf{x}_i)$  from the segmented bone surfaces. Since cortical bone tissue density differs significantly from cancellous bone tissue, the Hounsfield intensity at a surface location aids in delineating intact-surface from fracture-surface. In this step we take advantage of the fact that the vast majority of fracture surface in the metaphyseal region (near the joint surface) is from lower density bone. For both estimation and classification of the surface-point intensities we adopt a rationale which attempts to minimize the probability of mis-classifying an intact-surface (cortical bone) point as a fracture-surface (cancellous bone) point, i.e., we choose a threshold  $\tau$  to minimize type I errors in making the classification.



(a)

(b)

**Figure 3.** (a) High intensity circular regions depict thick cortical bone tissue from the proximal midshaft of the tibia. (b) More distally, there is much less contrast between cortical and cancellous bone tissue regions. This change in the contrast between cortical and cancellous tissue presents challenges in bone fragment segmentation and accurate fracture-surface point classification.

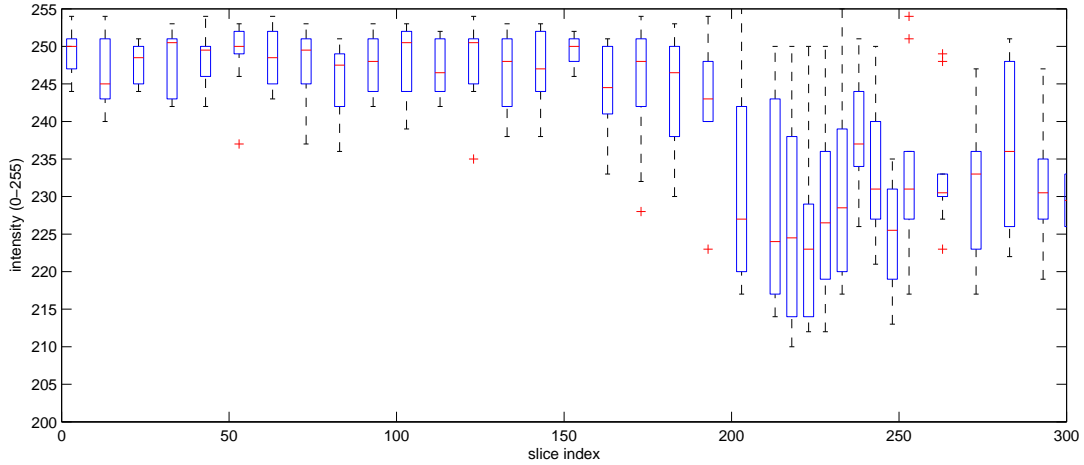


**Figure 4.** A boxplot of cortical tissue Hounsfield intensity as a function of slice index. Slice 0 denotes a slice from the bone mid-shaft and slice 260 denotes the last slice from the distal tibia that contains bone fragment voxels. Note that the variance of cortical tissue voxel intensities increases, and their median intensity value decreases, especially around slice 230 which is an area of difficulty for segmentation.

Typical long bones (such as the tibia and femur in the leg) consist of cortical bone tissue at the outer surface and cancellous bone tissue in the bone interior. Cortical bone tissue is very dense, typically having CT intensities  $\mathbf{I}(x, y, z) \in [900-1800]$  Hounsfield units. For the long bones of the lower extremity, as studied in this paper, this tissue is thickest along the bone mid-shaft and becomes very thin in metaphyseal regions near the articular joints. Cancellous tissue has varying density, typically having CT intensities  $\mathbf{I}(x, y, z) \in [500-1200]$  Hounsfield units. These bone density relationships are further complicated in the immediate vicinity of the articular joints (termed subchondral bone regions) where the specific functional demands produce a somewhat different bone structure at the macroscopic level.

As cancellous bone tissue typically has a substantially lower Hounsfield intensity than cortical bone tissue, and is found exclusively within the bone interior, we exploit the Hounsfield intensities in the vicinity of segmented surface points to distinguish between intact-surface points and fracture-surface points. This is a typical two-class problem to which there are well-known solutions.<sup>19</sup> Yet, there are two difficulties which make identification of fracture-surfaces on segmented bone surfaces a non-trivial problem:

1. Estimated surface locations from the surface segmentation may lie away from the true location of the cortical bone surface as shown in Figure 2.
2. Cortical bone tissue becomes very thin and less dense in distal and proximal regions of bones. Figure 3 shows CT slices that exhibit this behavior and Figure 4 provides a statistical analysis of this behavior as a function of location along the limb-bone shaft, starting at the mid-shaft (slice index 0) and extending to the fragments of the distal tibia (slice index 230).

These problems were addressed by estimating bone surface intensities and classifying them to minimize the possibility of mis-labeling an intact-surface point as a fracture-surface point. First, we address problem (1) by applying a standard  $9 \times 9 \times 9$   $max()$  filter as defined in standard image processing texts.<sup>20</sup> This provides a

conservatively-high estimate of the Hounsfield intensity at each surface point and assumes a maximum deviation of up to 4 pixels between the computed surface segmentation and the true bone surface. Second, we address problem (2) by minimizing the probability of mis-classifying an intact-surface point as a fracture-surface point, i.e., we choose a threshold  $\tau$  to minimize type I errors.

### 2.3. Fragment Surface Segmentation

To solve the binary classification problem, a mixture model consisting of two Gaussian probability distributions is fit to the histogram of estimated fragment surface intensities (see Figure 5(a)). As mentioned previously, a threshold  $\tau$  is selected to minimize type I errors for classification of the intact-surface intensities and subsequently applied for intact-surface / fracture-surface segmentation (see Figure 5(b)). The fracture surface is then the largest *contiguous* region of fracture-surface points resulting from the classification step (see Figure 5(c)). Note that two surface points  $\mathbf{x}_i$  and  $\mathbf{x}_j$  are members of a single contiguous fracture-surface region if there exists a path along edges of the surface mesh which connects  $\mathbf{x}_i$  and  $\mathbf{x}_j$  and only traverses points considered to be fracture-surface points.

### 2.4. Surface Alignment

For lack of a reliable 1-to-1 fracture surface classifier, we rely on minimal, yet necessary, user interaction. Here a user coarsely subdivides segmented fracture-surface regions into pairs of surfaces that are likely to, but need not exactly correspond. Using these fracture-surface pairs, a multi-body alignment scheme following that of Pulli<sup>8</sup> is applied, which uses a modified metric for the Iterative Closest Point (ICP)<sup>21</sup> fracture-surface alignment step. Our modification consists of two terms: (1) a point-to-plane Euclidean distance metric<sup>10</sup> and (2) an intensity matching metric.<sup>7,9</sup>

We align points on one surface to the other surface by minimizing the distance between the points on one surface to the plane defined by the nearest point and its associated normal on the other surface. For each point-to-plane distance being matched (and summed) there is a weighting coefficient as defined by the joint-likelihoods described below. This helps matched surfaces to join smoothly by emphasizing good matches at the perimeter.

$$e = \min_{\mathbf{R}, \mathbf{t}} \sum_{(i,j) \text{ pairs}} p(f(\mathbf{x}_i)|\omega_o)p(f(\mathbf{y}_j)|\omega_o) \|\mathbf{x}_i - \text{proj}_{\mathbf{n}_i}(\mathbf{R}\mathbf{y}_j + \mathbf{t})\|^2$$

Where  $\mathbf{R}$  is an unknown 3x3 rotation matrix,  $\mathbf{t}$  is a 3x1 translation vector,  $\text{proj}_{\mathbf{n}_i}(\mathbf{v})$  is the projection of vector  $\mathbf{v}$  into the plane defined by the point  $\mathbf{x}_i$  and its associated surface normal  $\mathbf{n}_i$  and  $p(f(\mathbf{x}_i)|\omega_o)p(f(\mathbf{y}_j)|\omega_o)$  is the joint-likelihood that the point pair  $(\mathbf{x}_i, \mathbf{y}_j)$  come from bone tissue close to the outer surface, i.e., the probability that the intensity observed at point  $\mathbf{x}_i$ ,  $f(\mathbf{x}_i)$ , comes from the cortical tissue class denoted here as class  $\omega_0$ .

This fusion of matching surface geometry and Hounsfield intensities is more robust than using geometry alone, as it takes into account the fact that surface estimates, i.e., segmentation results, tend to be more accurate in regions of high contrast in the CT data. In the case of comminuted bone fragment segmentation, the background consists mainly of soft tissue which has a low CT intensity  $\mathbf{I}(x, y, z) \in [0 - 600]$  Hounsfield units. Since cortical bone tissue regions have good contrast with respect to the soft tissue background, estimates of the shape and location of such regions are more accurate than the similar estimates of cancellous tissue regions. The term  $p(f(\mathbf{x}_i)|\omega_o)p(f(\mathbf{y}_j)|\omega_o)$  takes this into account by providing a weighting coefficient for each matched geometric point pair. The weighting is the product of the probability that each of the points within the matched point pair  $(\mathbf{x}_i, \mathbf{y}_j)$  comes from cortical tissue. This probability may be computed using the estimated distribution for the

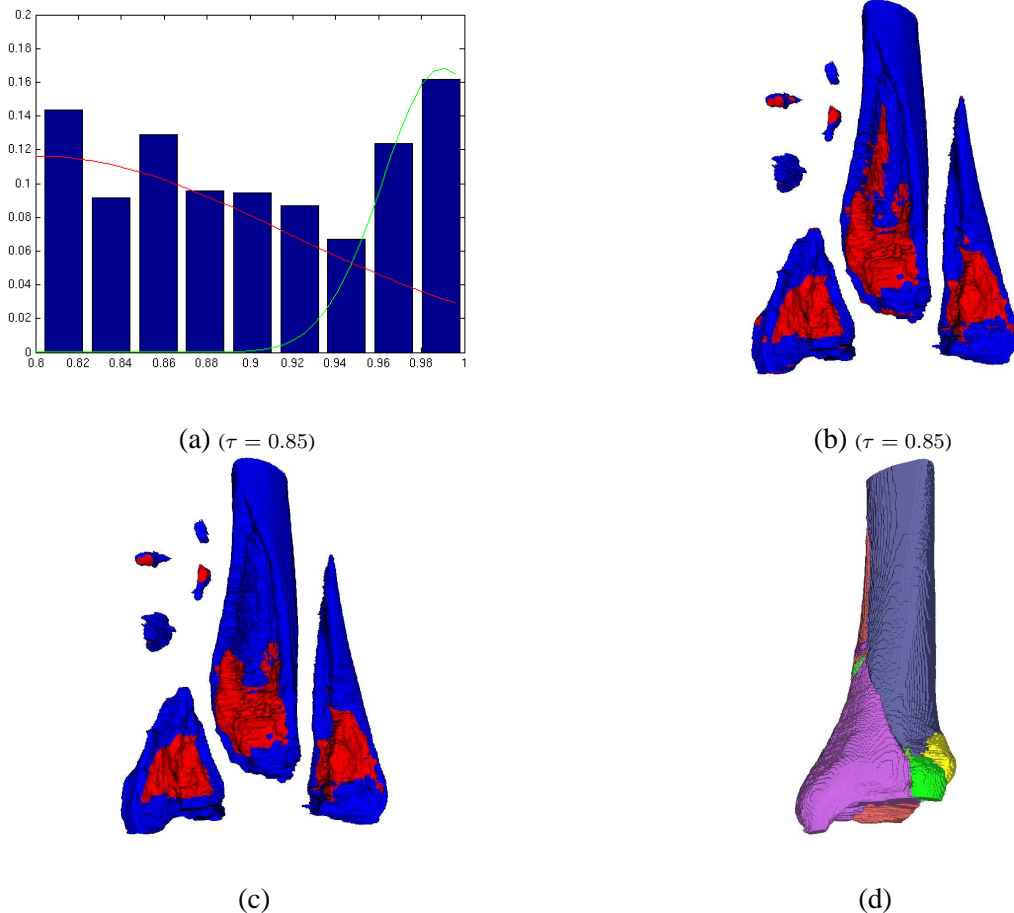


**Figure 5.** Segmenting fragment surfaces: (a) the normalized distribution of estimated Hounsfield intensities for the bone fragment surface points shown in (b,c). The distribution is seen as a mixture of two Gaussians and the fit Gaussians are plotted for cancellous tissue (shown in red) and cortical tissue (shown in green). A conservative threshold  $\tau = 0.85$  is chosen to minimize the probability of mis-classifying intact-surface points as coming from a fracture surface. (b) The resulting segmentation, where points classified as belonging to the intact-surface are shown as blue and fracture-surface points are shown as red. (c) The estimated fracture surfaces, i.e., the largest contiguous region of fracture-surface points on each fragment, are shown here. (d) An aligned reconstruction of the fragments demonstrates the excellent quality of the reconstruction – each fragment is colored differently (see §3 for details).

intensities of cortical surface points computed in §2.3 and shown as the rightmost curve in Figure 5(a). Since the intensity assumed by each surface point is considered to be independent and identically distributed with the estimated distribution from §2.3, the product  $p(f(\mathbf{x}_i)|\omega_o)p(f(\mathbf{y}_j)|\omega_o)$  is equivalent to  $p(f(\mathbf{x}_i), f(\mathbf{y}_j)|\omega_o)$ , which is the joint-likelihood that the intensities estimated for the point pair  $(\mathbf{x}_i, \mathbf{y}_j)$  are from cortical bone tissue, referred to as the class  $\omega_o$ . This coefficient is larger for matched point pairs with high Hounsfield intensities than those with lower Hounsfield intensities, which makes fragment alignments more sensitive to matched surface point pairs with high Hounsfield intensities.

### 3. RESULTS

Figure 6(a) shows an iso-surface representation of a tibial pilon fracture test case. The nature of the bone fragmentation results in the CT iso-surface being unable to discriminate between different bones, let alone between bone fragments. Using the segmentation algorithm from §2.1, eighteen bone fragments were identified

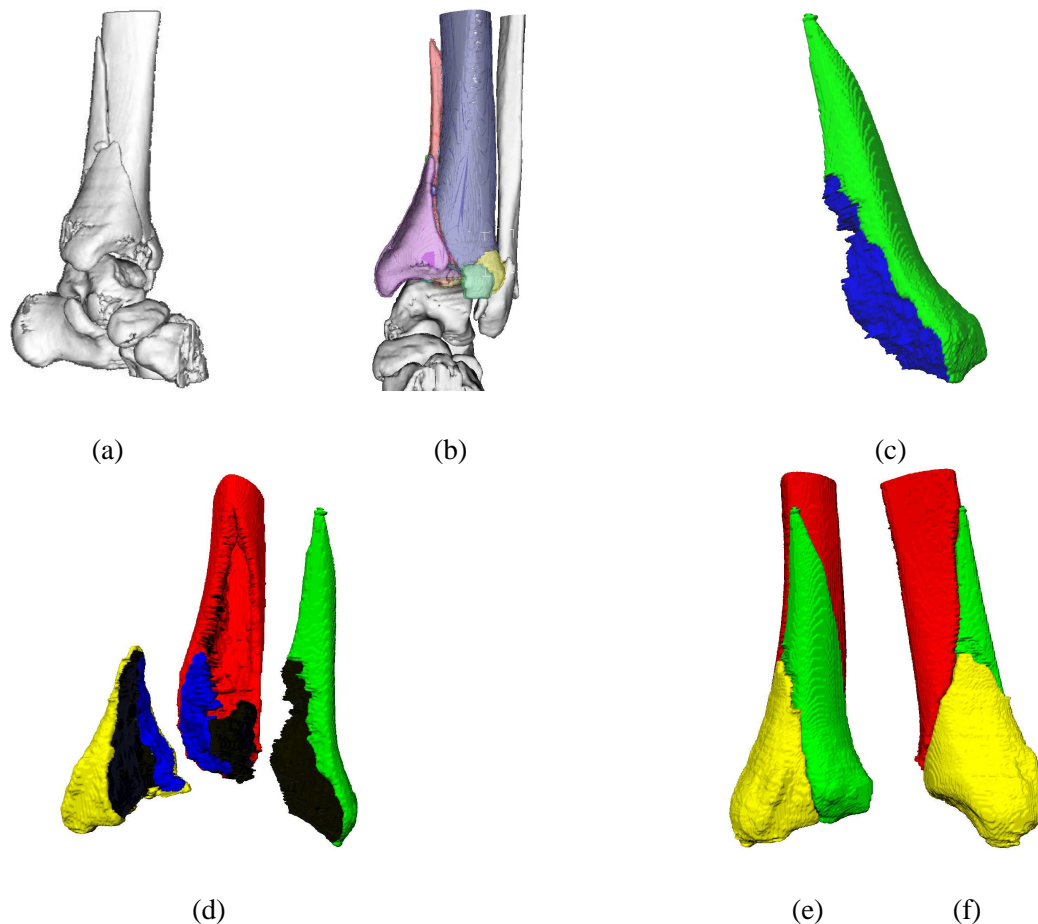


**Figure 6.** An overview of the fracture fragment identification and reconstruction system: (a) an iso-surface of a fractured tibia, (b) segmentation of the CT scan data generates discrete closed fragment surfaces shown in different colors (c) fragment surface points are then divided into intact-surface points (green) and fracture-surface points (blue) (d) fracture surfaces are subdivided interactively, here, black and blue regions denote sub-regions of various fragment's fracture-surface (e-f) two views of automatically aligned fracture-surface sub-regions using a multi-body surface alignment algorithm.

within the CT scan (Figure 6(b)). In this case there were 7 fragments with sufficient volume (size) to be deemed of clinical importance. Assembly of these 7 fragments took approximately 5 minutes of user interaction (Figure 6(c) and (d)), and just a few seconds of reconstruction alignment processing time (Figure 6(e) and (f)). The reconstruction obtained is excellent, as readily judged by its visual appearance.

#### 4. CONTRIBUTION

While intra-operative navigation tools exist to aid in reconstruction of long-bone fractures,<sup>11</sup> these systems are restricted to simple two-fragment fractures. The presented system represents the only example (to the authors' knowledge) of a system for computer-assisted 3D reconstruction of highly fragmented bone fractures. The system also represents a novel integration of bone fragment surface segmentation from CT data, bone fragment surface segmentation from Hounsfield intensities, and 3D surface registration techniques. Modifications were made to accommodate interactively solving the 1-to-1 correspondence problem for sub-regions of fragment

fracture surfaces. Common-practice multi-view registration techniques were fused with a new probabilistically inspired alignment error metric for reconstruction.

## 5. CONCLUSIONS

We have described a novel system for the semi-automatic reconstruction of highly fragmented bone fractures. The system represents the first fully-3D interactive reconstruction system available and is a logical extension of a system developed to reconstruct archaeological objects from their fragments. The system addresses difficult challenges related to the accuracy of segmented surface points and the fact that a single fracture surface on a fragment may correspond to many other fragments. The resulting system allows for a semi-automatic reconstruction of the bone fragments that is critical for providing good prognosis for these cases that are particularly difficult to reconstruct.

*This work was supported by grants from the NIH (AR046601 and AR048939) and the AO Foundation, Switzerland.*

## REFERENCES

1. J. L. Marsh, S. Bonar, J. V. Nepola, T. A. Decoster, and S. R. Hurwitz, "The use of an articulated external fixator for fractures of the tibial plafond," *Journal of Bone and Joint Surgery*, vol. 77A, pp. 1498–1509, 1995.
2. J. L. Marsh, D. P. Weigel, and D. R. Dirshl, "Tibial plafond fractures. how do these ankles function over time?," *Journal of Bone and Joint Surgery*, vol. 85A, pp. 287–295, 2003.
3. A. Praemer, S. Furner, and D. Rice, *Musculoskeletal Conditions in the United States*. Rosemont, IL: AAOS, 1999.
4. T. D. Brown, R. C. Johnston, C. L. Saltman, J. L. Marsh, and J. A. Buckwalter, "Posttraumatic osteoarthritis: a first estimate of incidence, prevalence, and burden of disease," *J Orthop Trauma*, vol. 20, no. 10, pp. 739–744, 2006.
5. W. Wells, P. Viola, H. Atsumi, S. Nakajima, and R. Kikinis, "Multi-modal volume registration by maximization of mutual information," *Medical Image Analysis*, vol. 1, no. 1, pp. 35–51, 1996.
6. K. Li, X. Wu, D. Chen, and M. Sonka, "Optimal surface segmentation in volumetric images – a graph-theoretic approach,"
7. A. Johnson and S. Kang, "Registration and integration of textured 3-d data," in *Proc. Int. Conf. on 3D Digital Imaging and Modeling*, pp. 279–290, 1994.
8. K. Pulli, "Multiview registration for large data sets," in *Proc. Int. Conf. on 3D Digital Imaging and Modeling*, pp. 160–168, 1999.
9. G. Godin, M. Rioux, and R. Baribeau, "Three-dimensional registration using range and intensity information," in *SPIE*, vol. Vol. 2350: Videometrics III, pp. 279–290, 1994.
10. Y. Chen and G. Medioni, "Object modelling by registration of multiple range images," *Image and Vision Computing*, vol. 10, pp. 145–155, 1992.
11. O. Ron, L. Joskowicz, A. Simkin, and C. Milgrom, "Computer-based periaxial rotation measurement for aligning fractured femur fragments: Method and preliminary results," *Lecture Notes in Computer Science*, no. 2208, pp. 17–23, 2001.
12. A. Willis, D. Cooper, *et al.*, "Bayesian Pot-Assembly from Fragments as Problems in Perceptual-Grouping and Geometric-Learning," in *ICPR*, vol. Vol. III, pp. 297–302, 2002.
13. G. Papaioannou, E.-A. Karabassi, and T. Theoharis, "Reconstruction of three-dimensional objects through matching of their parts," *IEEE Trans. on Pattern. Anal. and Mach. Intell.*, vol. 24, no. 1, pp. 114–124, 2002.
14. Q. Huang, S. Flöry, N. Gelfand, M. Hofer, and H. Pottmann, "Reassembling fractured objects by geometric matching," in *Proc. of SIGGRAPH*, (Boston, USA), July 2006.
15. Konika Minolta, Sakai, Osaka Japan, *VIVID 910 Non-Contact 3D Digitizer*, 2006.
16. ShapeGrabber Inc., Ottawa, Canada, *PRM330 3D Digitizer*.
17. D. D. Anderson, V. Muehling, J. Marsh, and T. Brown, "Precise identification of bone fragment boundaries to assist in reduction of highly comminuted fractures," *Computer-Aided Surgery*, vol. 9, no. 3, p. 116, 2004.

18. C. Beardsley, C. Bertsch, J. Marsh, and T. Brown, "Interfragmentary surface area as an index of comminution energy: proof of concept in a bone fracture surrogate," *Journal of Biomechanics*, vol. 35, no. 3, pp. 331–338, 2002.
19. R. O. Duda, P. E. Hart, and D. G. Stork, *Pattern Classification*. Wiley-Interscience, 2nd ed. ed., 2000.
20. R. C. Gonzalez and R. E. Woods, *Image Processing*. Prentice Hall, 2nd ed. ed., 2000.
21. P. Besl and N. McKay, "A Method for Registration of 3-D Shapes," *PAMI*, vol. 14, no. 2, pp. 239–256, 1992.